Journal of Materials Chemistry A

Accepted Manuscript

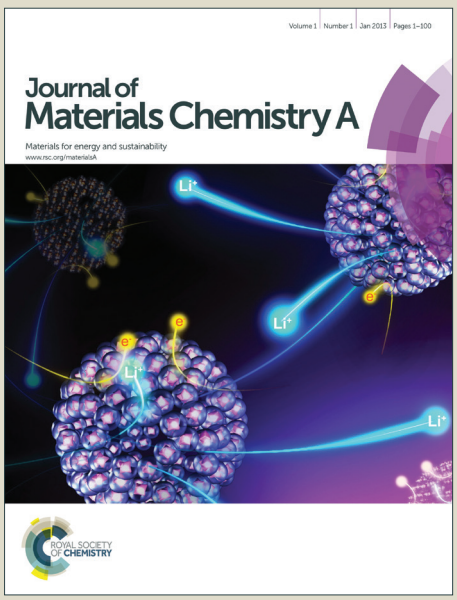

ROYAL SOCIETY OF CHEMISTRY

www.rsc.org/materialsA

Graphical Abstract

Journal of Materials Chemistry A

Description	A pH-mediated approach to synthesize single crystalline $LiMn_2O_4$ is developed by truncating a small portion of surfaces to support Li diffusion while leaving most remaining surfaces with minimal Mn dissolution, enabling $LiMn_2O_4$ with superior lithium storage properties.
Title	**Facile pH-mediated synthesis of morphology-tunable $MnCO_3$ and their transformation to truncated octahedral spinel $LiMn_2O_4$ cathode materials for superior lithium storage**
Authors	Sisi Huang, Hao Wu*, Penghui Chen, Yi Guo, Bo Nie, Baojun Chen, Heng Liu and Yun Zhang*

Graphical Information

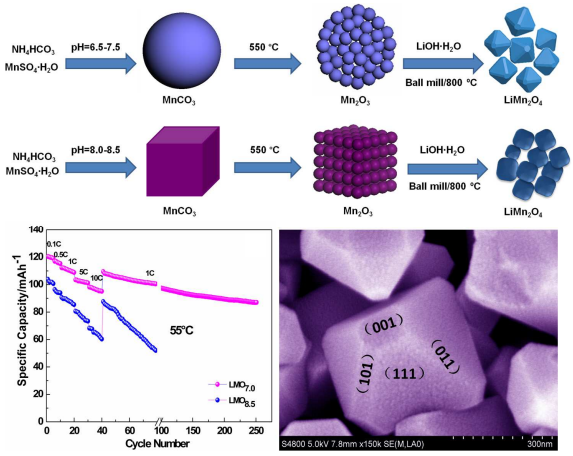

Journal Name

RSCPublishing

ARTICLE

Facile pH-mediated synthesis of morphology-tunable $MnCO_3$ and their transformation to truncated octahedral spinel $LiMn_2O_4$ cathode materials for superior lithium storage

Cite this: DOI: 10.1039/xoxxoooooox

Received ooth January 2012,
Accepted ooth January 2012

DOI: 10.1039/xoxxoooooox

www.rsc.org/

Sisi Huang, Hao Wu*, Penghui Chen, Yi Guo, Bo Nie, Baojun Chen, Heng Liu and Yun Zhang*

Diverse single crystalline spinel $LiMn_2O_4$ cathode materials are prepared deriving from spherical and cubic $MnCO_3$ as precursors obtained by a general pH-mediated chemical precipitation approach. With careful pre-controls over the particle properties of $MnCO_3$ precursors upon pH adjustment, five $LiMn_2O_4$ samples with average size of 0.5-1.0 μm are prepared. Among these samples, the $LiMn_2O_4$ prepared at pH value of 7.0 exhibits a well-defined truncated octahedral crystal structure, in which most surfaces are aligned to the {111} crystalline orientations with minimal Mn dissolution, while a small portion of the structure is truncated along the {110} orientations to support Li diffusion. Benefiting from the unique crystal structure, the synthesized $LiMn_2O_4$ as cathode manifests superior rate capability and prolonged cycle stability, especially at elevated temperatures: the capacity retention of 86.7% after 1000 cycles at 5C under 25 ℃ and of 80.7% after 250 cycles with 1C under 55 ℃. These results demonstrate that the morphology of $MnCO_3$ precursor prepared by precipitation method has a significant influence on the crystal structure and electrochemical properties of resultant $LiMn_2O_4$. The work described here also shows a great potential in practical industrial application toward developing high performance $LiMn_2O_4$ electrode materials for lithium ion batteries.

Introduction

Rechargeable lithium-ion batteries (LIBs) have achieved a great success as main power sources for portable electronic devices due to their high energy density and long cycle life. Current demands for LIBs have been increasingly transferring from small portable power to large-scale energy storage system for applications in electric vehicles (EVs) and hybrid electric vehicles (HEVs).[1-2,37-38] In order to achieve the commercialization of LIBs for EVs and HEVs, tremendous efforts have been devoted to develop better cathode materials with high energy and power. As one of the alternatives to currently commercialized $LiCoO_2$, spinel $LiMn_2O_4$ is considered to be one of the most competitive candidates of cathode materials to be used for EVs and HEVs due to its wealthy merits of low cost, environmental friendliness, high abundance and good safety.[3] However, bulk $LiMn_2O_4$ powders obtained by conventional solid-state preparation method still bear some drawbacks such as rapid capacity fading during cycling, which mainly results from Mn dissolution via a disproportionation reaction ($2Mn^{3+} \rightarrow Mn^{2+} + Mn^{4+}$) and structural transformation from cubic to tetragonal phase, induced by Jahn–Teller distortion of Mn(III).[4-7,39] Coating with electrochemically inert oxides and phosphates has been recognized as an important approach to improve the electrochemical performances of $LiMn_2O_4$. Nevertheless, coating materials are generally unfavourable for both Li-ion conduction of cathode materials and interfacial charge transfer of the electrode, not only because they behave as insulators for Li-ion conduction, but also because they increase Li-ion diffusion length resulting in deterioration of electrochemical performance.[8]

Another effective approach to ameliorate the electrochemical properties of $LiMn_2O_4$ cathode material is synthesis of diverse nanostructured $LiMn_2O_4$ materials including nanoparticles,[9] nanorods,[10] nanowires,[11] nanotubes,[12] porous sphere,[13,40] and hollow microspheres.[14] The advantages of these nanosized $LiMn_2O_4$ electrode materials, such as shorter length for both electronic and ionic transport, higher electrode/electrolyte contact area, enable better power performance as compared to bulk electrode for LIBs.[2,15,16] For example, nanoparticles-assembled porous $LiMn_2O_4$ synthesized by Yang et al. exhibit 73.3% capacity retention after 1000 cycles at room temperature and 77.3% after 100 cycles at 60 ℃.[17] Kun and co-workers reported that nanoparticulate $LiMn_2O_4$ has a high initial discharge specific capacity of 122.5 mAh g^{-1}.[18] However, nanosized $LiMn_2O_4$ particles have many irreversible sites for Li insertion, such as dangling bonds and surface disordering, whilst their extremely large surface-to-volume ratio could

conversely promote the dissolution of manganese into acid impurity-containing electrolyte at high-voltage region, thus resulting in instable cycle life.[19-21] For instance, Jiao et al. reported that nanoparticulate $Li_xMn_yO_4$ materials showed much more severe capacity fading during cycling than bulk and micron-sized mesoporous $Li_xMn_yO_4$ materials.[22] Another disadvantage of nanosized $LiMn_2O_4$ materials is that they cannot be packed as densely on the current collector if their particles were downsized within 100 nm; this fact means that electrodes made of nanoscale $LiMn_2O_4$ particles have a high porosity, thus leading to a decrease in the cell capacity.[3, 23]

Taking these issues into consideration, synthesis of spinel $LiMn_2O_4$ materials with submicron particle size (0.1-1.0 μm) appears to be an efficient and practical solution since in addition to increasing the volumetric energy density of $LiMn_2O_4$ cathode materials, large dimension of particles could provide an additional advantage to minimize their surface area leading to reduce side reactions and irreversible capacity.[24,25] On the other hand, the structure stability and cycle life of $LiMn_2O_4$ is tightly related to their crystal structure because Mn dissolution is believed to be largely dependent on the crystalline orientation of the surface exposed to the electrolytes. Spinel $LiMn_2O_4$ contains {100}, {110} and {111} crystal facets that have different surface energies and exhibit different stabilities. The {100} and {110} facets whose orientation are aligned to Li diffusion channels are most vulnerable to Mn dissolution, whereas the {111} facets, on which Mn atoms are most densely packed, has the lowest surface energy and exhibits the best stability. Recently, Kim et al. developed a novel crystal structure of spinel $LiMn_2O_4$, namely, a truncated octahedron, which have most exposed {111} crystal surface together with a small portion of truncated surfaces along the {110} and {100} crystalline orientations.[26] This unique crystal structure not only endow the $LiMn_2O_4$ with minimal Mn dissolution, but also retain the channels to support Li diffusion, thus giving rise to better power and cycling performance than its non-truncated octahedral counterpart which only contains {111} surfaces. However, such a unique crystal structure of $LiMn_2O_4$ was fabricated in their study by using a hydrothermal approach with a high synthetic temperature of 220 ℃, which is an extremely harsh synthetic process, thus being not applicable to the practical industrial production. Moreover, conventional synthetic methods like solid-state reaction are hard to achieve this goal because of its intrinsic drawbacks in careful control over the nucleation and growth of $LiMn_2O_4$ crystals.[27,28] In this regard, it still remains a great challenge to develop new synthetic methods for facile and large-scale production of spinel $LiMn_2O_4$ with well-designed particle size and crystal structure, as well as excellent electrochemical performance.

Herein, we attempt to synthesize high-performance spinel $LiMn_2O_4$ cathode materials deriving from spherical and cubic $MnCO_3$ as precursors prepared by a general and simple pH-mediated precipitation method. With careful pre-controls over the particle size and morphology of $MnCO_3$ precursors upon pH adjustment, five samples of $LiMn_2O_4$ (denoted as LMO_x, x represent pH value of 6.5, 7.0, 7.5, 8.0, and 8.5, respectively) with average size of 0.5-1.0 μm can be prepared through reaction between $LiOH·H_2O$ and porous Mn_2O_3 spheres and cubes obtained from complete decomposition of $MnCO_3$ precursors. It is demonstrated that the $LMO_{7.0}$ sample with an average particle size of ~0.8 μm exhibits a well-defined truncated octahedral structure in which most surfaces are aligned to the crystalline orientations of {111} facets activating minimal Mn dissolution, while a small portion of the structure is truncated along the {110} orientations to support the Li diffusion. As compared to the samples prepared at relatively higher pH value, the truncated octahedral structure of $LMO_{7.0}$ bears multiple lattice orientations within a single crystal framework. As a result, the $LMO_{7.0}$ exhibits superior rate capabiliy and prolonged cycle stability, especially at elevated temperatures, when used as cathode materials for LIBs.

Experimental

Materials synthesis

Preparation of Spherical and Cubic $MnCO_3$: NH_4HCO_3 (21.0%, AR), $LiOH·H_2O$ (99.0%, AR), $NH_3·H_2O$ (25%, AR) and ethanol (99.7%, AR) were purchased from Sigma-Aldrich. $MnSO_4·H_2O$ (99.0%, AR) and MnO_2 (99.0%, AR) was supplied by TianJin ZhiYuan Reagent Co. Ltd. All reagents were used without further purification. The spherical and cubic $MnCO_3$ precursors were firstly prepared by a simple pH-mediated precipitation method. Typically, 0.3 mol NH_4HCO_3 were dissolved in 500 mL deionized water to form a mixture solution, signed as A. Then, 0.03 mol $MnSO_4·H_2O$ were dissolved in 500 mL deionized water, followed by adding 20 mL ethanol to obtain another mixture solution, signed as B. After that, the solution of A and B were pumped together into a flat bottle flask under vigorous stirring to precipitate at room temperature, and a certain amount of $NH_3·H_2O$ as complexing agent was then added drop by drop to adjust the pH value of the suspension at 6.5, 7.0, 7.5, 8.0, and 8.5, respectively. The as-prepared suspension was subsequently maintained at 25 ℃ overnight, followed by filtration, washing, and drying to obtain spherical and cubic $MnCO_3$ precursors.

Preparation of $LiMn_2O_4$: As for preparation of $LiMn_2O_4$, the as-obtained $MnCO_3$ precursors were firstly pre-sintered at 550 ℃ for 4 hours to form porous Mn_2O_3 intermediates. Subsequently, the porous Mn_2O_3 intermediates were mixed thoroughly with $LiOH·H_2O$ in the molar ratio of Li: Mn = 1.05:2. After mixing and ball-milling for 10 min, the mixture was preheated to at 480 ℃ (melting point of $LiOH·H_2O$) for 4 h in air, followed by calcinating at 800 ℃ for 12 h to finally get $LiMn_2O_4$ powders.

Solid-state Reaction Preparation of $LiMn_2O_4$: For comparison, conventional solid-state reaction combined with ball-milling was also carried out to prepare spinel $LiMn_2O_4$ sample (denoted as LMO-S) by using MnO_2 and $LiOH·H_2O$ as starting materials, sintering at 800 ℃ for 12 h.

Material characterization

X-ray diffraction (XRD) analysis was employed to identify the crystal structure of samples by using a Bruker DX-1000 diffractometer with Cu-Kα radiation in the 2θ angular range of 10 ~ 70 ° at a scanning rate of 0.02 $°s^{-1}$. The particle morphologies of $MnCO_3$, Mn_2O_3 and $LiMn_2O_4$ were observed by using scanning electron microscopy (SEM, JSM-5900, Japan) and field emission transmission electron microscopy (FE-TEM, 200kV, Tecnai G2 F20, FEI, Netherlands) and high-resolution TEM (HRTEM) equipped with a selected area electronic diffraction (SEAD). N_2 adsorption measurements were performed with Tristar 3020 instrument (Micromeritics) to determine the specific surface area and pore structure parameters of LMO_x products.

Electrochemical measurements

The electrochemical properties of $LiMn_2O_4$ were tested by CR2032 coin-type cell. The working electrodes were fabricated by dispersing 80 wt.% $LiMn_2O_4$ powders (active materials), 15 wt.% black carbon (conductive materials), and 5 wt.% PVDF (binder) in N-methyl-2-pyrrolidone (NMP) solvent to form a homogeneous slurry. Then the

slurry was coated on an Al foil current collector and dried at 120 ℃ for 10 h in a vacuum oven. All electrodes were cut into disks with a diameter of 10 mm, the average mass loading of which was about 2.0 mg cm^{-2}. After that, CR-2032 coin-type cells were assembled in an argon-filled glove box by utilizing the above prepared disks as cathode, metal lithium foils as anode, polypropylene micro-porous films (Celgard 2400) as separator, and 1M $LiPF_6$ dissolved in a mixture of ethylene carbonate (EC) and dimethyl carbonate (DMC) and diethyl carbonate (DEC) (1:1:1 in volume) as electrolyte. Galvanostatic charge and discharge tests were conducted in a potential range of 3.0 ~ 4.3 V (*vs.* Li/Li^+) at room temperature using a battery system (Neware CT-3008W battery tester, China). The Electrochemical impedance spectroscopy (EIS) tests were performed by the CHI600D electrochemical workstation with the scanning rate of 0.1 mV/s in the voltage range of 3.0~4.3 V.

Results and discussion

XRD was performed to identify the crystallographic structure and crystallinity of the synthesized products, and the results obtained are presented in Fig. 1. As shown in Fig. 1a, all the $MnCO_3$ samples prepared at different pH condition exhibit a pure hexagonal phase (PDF#44-1472), indicative of the high purity of the precursors. Fig. 1b (upper) displays the XRD patterns of LMO_x products, in which all the peaks of the five samples are corresponding to the standard pattern of spinel $LiMn_2O_4$ (PDF#35-0782). All the five samples can be identified as a single pure phase of cubic spinel structure in the space group Fd3m, in which the lithium ions occupy the tetrahedral (8a) site and manganese metal ions reside at the octahedral (16d) site. Notably, no peaks of the cubic Mn_2O_3 phase (PDF#24-0508) and other impurities are detected in the final LMO_x products, suggesting the complete conversion of Mn_2O_3 intermediates with lithium salts to spinel $LiMn_2O_4$.

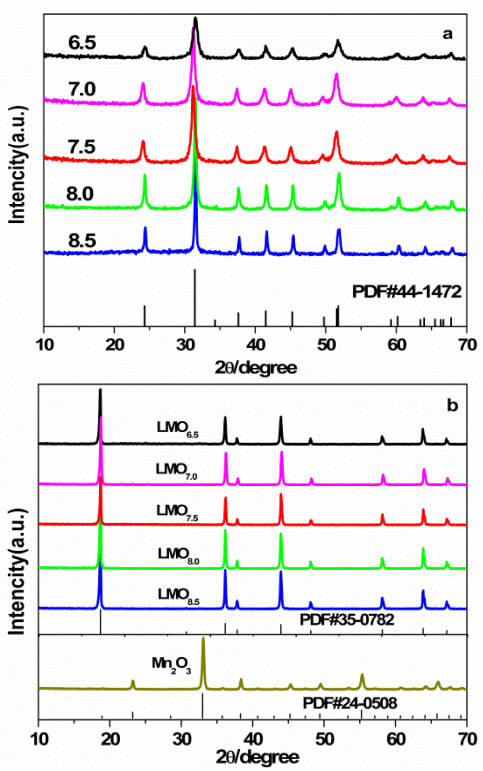

Fig. 1 XRD patterns of prepared (a) $MnCO_3$, (b, below) Mn_2O_3 and (b, upper) LMO_x

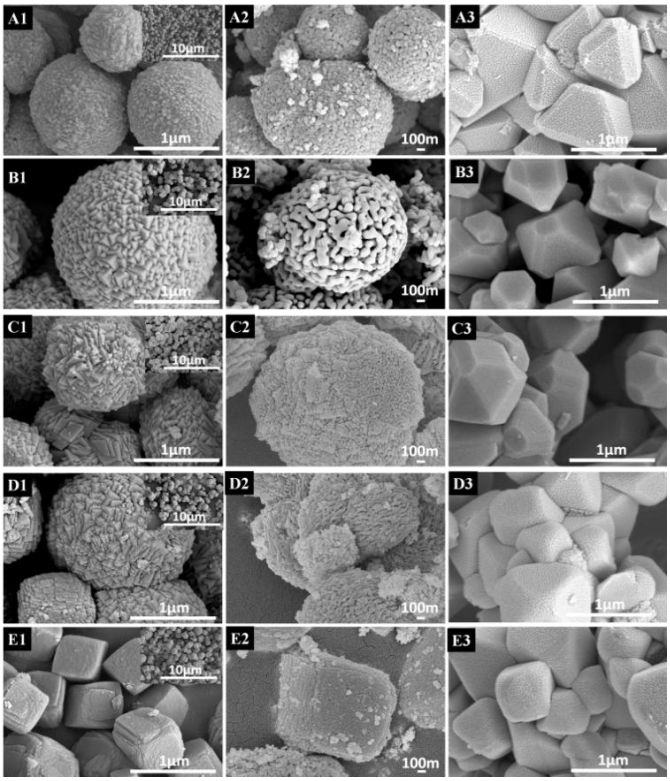

Fig. 2 SEM images of (A1-E1) $MnCO_3$, (A2-E2) Mn_2O_3, and (A3-E3) LMO_x prepared at different pH of 6.5 (A1-5), 7.0 (B1-5), 7.5 (C1-5), 8.0 (D1-5), and 8.5 (E1-5).

Fig. 2 presents the typical SEM images of prepared $MnCO_3$ precursors, Mn_2O_3 intermediates and corresponding LMO_x products. As shown in Fig. 2A-E1, it is clearly discerned that the particle size and morphology of $MnCO_3$ precursors have a dependence on the pH condition during the $MnCO_3$ precipitation. Through the control of pH from 6.5 to 8.5, uniform and monodispersed $MnCO_3$ with spherical and cubic morphology can be prepared. Interestingly, the spherical $MnCO_3$ precursors with rough surface which is compactly stacked with flaked primary particles tend to be obtained at relatively low pH of 6.5 and 7.5, whereas the particle size of $MnCO_3$ precursors increases with increasing the pH value from 7.5 to 8.5, and their morphology also gradually transforms from spheres to cubes. This phenomenon may be ascribed to that the quantity ratio of OH^- to H^+ ions in solution is varying along with adjusting pH value, which determines the dissimilar distribution of surface charges on different crystallographic planes of $MnCO_3$ crystals, thereby leading to different growth directions and stacking behaviors of microcrystallines, and as a result, generating diverse size and morphology in the resultant $MnCO_3$ particles.[31]

After thermal decomposition of $MnCO_3$, the obtained Mn_2O_3 intermediates inherit the spherical and cubic shape of $MnCO_3$, but they are highly porous and consisted of quasi-round primary nanoparticles with 50-200 nm, as clearly seen in Fig. 2A2–E2. The porous structure is attributed to the CO_2 evolution from the $MnCO_3$ bulk during the thermal decomposition of $MnCO_3$ to form manganese oxide.[14] It should be noted from Fig 2B2 that the obtained Mn_2O_3 based on pH value of 7.0 has more loose structure than other samples, which would produce a potential effect on the particle morphology of its corresponding $LiMn_2O_4$ product. Fig. 2A3–E3 further present the morphologies of LMO_x obtained by

sintering porous Mn_2O_3 impregnated with lithium salt. It is demonstrated that the morphologies of Mn_2O_3 intermediates are not inherited by final LMO_x products, but instead by diamond-like $LiMn_2O_4$ particles with a range of 0.4~1.2 μm in size dimension. It should be pointed out that although the particle size of the synthesized $MnCO_3$ precursors is highly dependent on the pH value in chemical precipitation, there is a tiny influence of the pH value on the $LiMn_2O_4$ particle size of final LMO_x products. However, comparing with the samples of $LMO_{8.0}$ and $LMO_{8.5}$, a well-defined octahedral morphology can be clearly distinguished in the samples of $LMO_{6.5}$, $LMO_{7.0}$ and $LMO_{7.5}$, among which $LMO_{7.0}$ and $LMO_{7.5}$ display a characteristic truncated octahedral crystal structure.

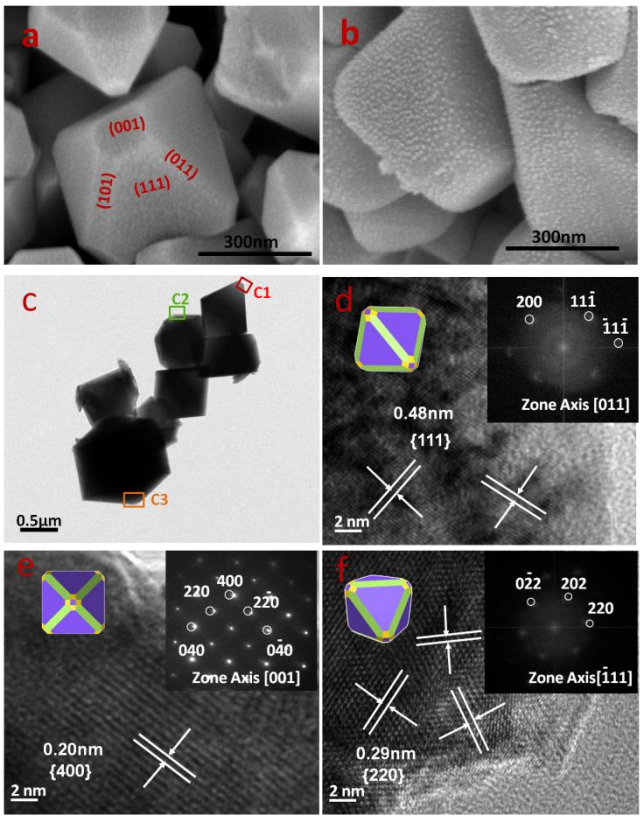

Fig. 3 SEM images of (a) $LMO_{7.0}$ and (b) $LMO_{8.5}$ at high magnification. (c) TEM images of $LMO_{7.0}$. (d-f) HRTEM images taken from selected regions marked as C1-C3 in c. Each HRTEM image of d-f taken from its corresponding region of C1-C3. The HRTEM images taken at different orientations as indicated by structural schematics in d-f. Inset of d-f shows the FFT pattern derived from each HRTEM image.

Moreover, the SEM images of $LMO_{7.0}$ at high magnification in Fig. 3a clearly visualize the truncated surfaces at the vertices and edges of the parental octahedral structure. Specifically, in addition to the dominant {111} surfaces, the orientation of the truncated surfaces at each vertex and edge can be reasonably assigned to {100} and {110} crystal facets, respectively, according to the established face orientation of the octahedral framework,[29] as well as those of its truncated derivatives.[30] However, the octahedral structure is hardly obtained if increasing the pH value above 7.5. The SEM images of the samples of $LMO_{8.0}$ and $LMO_{8.5}$ (Fig. 2D3 and E3; Fig. 3b) demonstrate that the edges of the crystals became indistinct and their particle morphologies tend to be of roundness rather than octahedron. Notably, almost all the synthesized LMO_x samples display an obvious particle agglomeration with each other, in which the particles with the truncated octahedral crystal structure seems to be easier to agglomerate through face-to-face interaction.

In order to investigate the detailed morphological and structural features of the LMO_x products, it is reasonable to look into the TEM images of the sample $LMO_{7.0}$, which are presented in Fig. 3. A typical TEM image of randomly selected particles in $LMO_{7.0}$, as shown in Fig. 3c, demonstrates that they have a truncated octahedral structure and their average particle size is estimated to be ~0.8 μm. Further TEM characterization conducted at various orientations also support the assigned truncated crystal structure marked in Fig. 3a. For the TEM observation at each orientation (see structural schematics in Fig 3d–f), a HRTEM image, the resultant Fast Fourier-transformed (FFT) pattern (insets on Fig. 3d–f), and the zone axis are attained. For example, when viewed along the direction normal to the truncated edge surface (Fig. 3d), a HRTEM image shows lattice fringes with a lattice distance of 0.48 nm along the {111} directions. The FFT pattern obtained from the HRTEM image exhibits spots that correspond to the lattice orientations as denoted in the inset. Also, the FFT pattern indicates the zone axis of the electron-beam is along the [011] direction, which is consistent with the orientation of the truncated surface. Similarly, when viewed along the directions normal to the truncated vertex surface (Fig. 3e) and the octahedral surface (Fig. 3f), lattice fringes along the {400} and {220} directions are observed, respectively. Moreover, the resultant zone axis is consistent with the orientation of each truncated surface. All these observations indicate that $LMO_{7.0}$ has a well-defined truncated octahedral structure, bearing multiple lattice orientations within a single crystal framework.

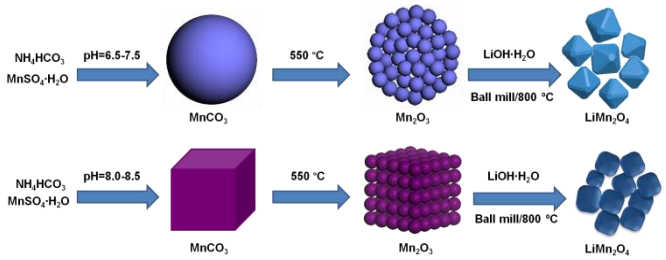

Fig. 4 Schematic illustration of formation process of spinel $LiMn_2O_4$.

The formation process of $LiMn_2O_4$ is illustrated in Fig. 4. A facile pH-mediated chemical precipitation method is first performed to prepare $MnCO_3$ precursors with different morphology. Spherical $MnCO_3$ is prone to obtain at relatively lower pH condition (6.5~7.5), whereas the morphology of $MnCO_3$ transforms to cubic shape with increasing the pH value (7.5~8.5). Subsequent thermal decomposition of the $MnCO_3$ precursors generates porous Mn_2O_3 intermediates with inherited spherical and cubic morphology from $MnCO_3$. To obtain $LiMn_2O_4$, the porous Mn_2O_3 intermediates impregnated with $LiOH{\cdot}H_2O$ were subjected to ball-milling, followed by sintering at 800 ℃. The highly porous structure of Mn_2O_3 is beneficial to the impregnation of the lithium salt, while the high temperature and the highly crystalline Mn_2O_3 favour the formation of spinel $LiMn_2O_4$. It is well known that the {111} facets is a major growth orientation of the $LiMn_2O_4$ particles when synthesized from a solid state reaction because the formation of {111} crystal facets is closely related to the lowest surface energy of the {111} surfaces. However, in our work, the $LiMn_2O_4$ products derived from $MnCO_3$ as precursor, which are obtained at relatively low pH condition (6.5~7.5), exhibit a truncated octahedral structure, in which most surface are aligned to the {111} crystalline

orientations with a small portion of truncated {110} and {100} surfaces. This fact demonstrates that in addition to the effect of sintering temperature, the morphology of $MnCO_3$ precursor prepared through the chemical precipitation approach also has a great potential influence on the particle morphology and crystal structure of the resultant spinel $LiMn_2O_4$.

The electrochemical performances of the as-prepared LMO_x products as cathodes were evaluated by using a coin-type cell. Fig. 5A shows the typical first charge/discharge curves of the LMO_x cathode materials at 0.1C rate (1C = 148 mA g^{-1}) between 3.0 and 4.3 V. As clearly seen, the first discharge capacities of $LMO_{6.5}$, $LMO_{7.0}$ and $LMO_{7.5}$ approach to about 117 mAh g^{-1} and this value gradually declines in $LMO_{8.0}$ (110 mAh g^{-1}) and $LMO_{8.5}$ (104 mAh g^{-1}). In the samples of LMO_x (x= 6.5, 7.0, 7.5), there are two evident potential plateaus at around 4.0 and 4.1 V for both charge and discharge curves, which are the typical electrochemical behavior of spinel $LiMn_2O_4$ with two-phase transition of λ-MnO_2/$Li_{0.5}Mn_2O_4$ at about 4.1 V vs. Li/Li^+ and $Li_{0.5}Mn_2O_4/LiMn_2O_4$ at about 3.9 V vs. Li/Li^+, respectively.[28] However, both of the plateaus in $LMO_{8.0}$ and $LMO_{8.5}$ are blurred, and their discharge plateaus shift to lower potential owing to the increased electrochemical polarization. Also, both the two samples clearly show relatively lower specific capacities than that of other three samples under the same condition, mainly due to their irregular particle morphology and undefined crystal structure, as shown in Fig. 2D3 and E3.

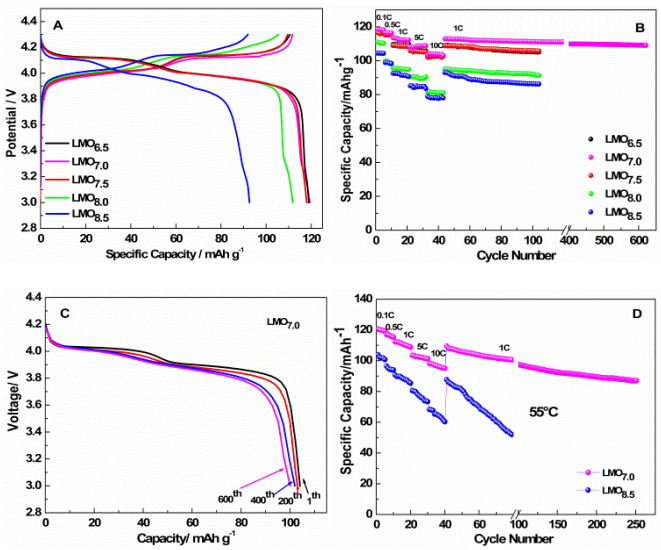

Fig. 5 Electrochemical performance of LMO_x products: (A) Initial charge/discharge profiles at a current rate of 0.1C. (B) Rate capabilities under variable current rate and cycle performances. (C) Typical discharge profiles of $LMO_{7.0}$ at different cycles. (D) Rate and cycle performances of $LMO_{7.0}$ and $LMO_{8.5}$ at 55 ℃. All measurement were conducted in the voltage range of 3.0-4.3 V *vs.* Li/Li^+.

To evaluate the rate capabilities, the five samples were successively cycled for 5 cycles at current rates ranging from 0.1 to 0.5C, and cycled for 10 cycles at current rates ranging from 1 to 10C. Fig. 5B presents the results obtained. All the samples show decreased capacities at high rates as the increase of current rate, due to the increase of cell polarization at high current,[32] indicating the diffusion-controlled kinetic process for the electrode reactions of $LiMn_2O_4$ materials. Clearly, in comparison with $LMO_{8.0}$ and $LMO_{8.5}$, the LMO_x samples obtained at relatively lower pH condition (6.5~7.5) demonstrates an obviously lower fading rate with increasing discharge rates, revealing their good reversibility during the Li^+ ion intercalation/deintercalation process. Specifically, at a low current rate of 0.1C, the discharge capacities of the $LMO_{7.0}$ and $LMO_{8.5}$ are 117 and 104 mAh g^{-1}, respectively. As the increase of current rates, the $LMO_{7.0}$ delivers 108 mAh g^{-1} at 5C and 103 mAh g^{-1} at 10C, showing 92.5 % and 88.4 % capacity retention, respectively, whereas the $LMO_{8.5}$ merely delivers 85 mAh g^{-1} at 5C and 79 mAh g^{-1} at 10C, corresponding to a capacity retention of 81.5 % and 75.6 %, respectively. Moreover, the capacities of the five samples are recovered to around 109, 113, 109, 95 and 92 mAh g^{-1}, respectively, when the current rate was decreased to 1C after having been cycled at higher current rate, indicating their good reversibility and good structure stability. Apparently, the LMO_x samples obtained at lower pH condition possess better initial capacity and rate capability than $LMO_{8.0}$ and $LMO_{8.5}$. Furthermore, the galvanostatic cycle tests continue to carry out for 60 cycles at 1C. After 60 charge/discharge cycles, the capacity retention for all the five samples is approaching to or exceeding 93.0 %. Notably, the $LMO_{7.0}$ shows the best cycling performance among all the five samples, achieving 97.1 % of its initial capacity. In addition, as compared to the LMO_x samples, the LMO-S sample prepared by a solid-state reaction approach shows inferior rate capability and cycle stability (Fig. S1, ESI†), mainly due to its irregular particle size and morphology (Fig. S2, ESI†) resulted from the uncontrolled crystal growth of $LiMn_2O_4$ within this synthetic process.

Fig. 5C further presents the 1st, 200st, 400st and 600st discharge curves of the $LMO_{7.0}$ electrode. The potential plateaus of the $LMO_{7.0}$ gradually changes during the charge/discharge progress. Two distinguish potential plateaus can be clearly observed at about 4.0 and 3.9 V after the first cycle and 600 cycles, suggesting that $LMO_{7.0}$ remains superior Li^+ ion intercalation/deintercalation reversibility. Although the potential plateau shifts to lower value after 600 cycles, consistent with the electrochemical behavior of $LiMn_2O_4$ caused by the electrochemical polarization during cycling, the $LMO_{7.0}$ electrode still delivery a capacity as high as 103 mAh g^{-1} with a capacity retention more than 90.0 % of its initial capacity at 1C, indicating its remarkable long-term cycling stability. It is generally known that the Mn dissolution tends to form unstable solid electrolyte interphase (SEI) layers on the electrode surfaces and is thus very critical for the cycle lives of $LiMn_2O_4$ cathodes.[33] Also, it should be noted that the Mn dissolution is largely dependent on the crystalline orientation of the surface exposed to the electrolyte. Since no compositional modification (e.g., cationic substitution with Co, Ni, Al, etc.) or surface treatment (e.g., oxide coating) has been adopted in our case, the excellent rate performance and cycling stability of the synthesized $LMO_{7.0}$ could be attributed to its unique particle properties and crystalline structures. Compared with other samples, $LMO_{7.0}$ possesses a well-defined truncated octahedral crystal structure, in which most surfaces are aligned to the {111} crystalline orientations with minimal Mn dissolution, while a small portion of the structure is truncated along the {110} orientations to support Li diffusion. Due to the unique crystal structure, the $LMO_{7.0}$ as electrode material exhibits much better rate capability and cycle performance than $LMO_{8.5}$ which has a poor crystal structure that might lead to severe Mn dissolution. On the other hand, highly porous structure of cathode materials would help to promote the diffusion of Li^+ ion in and out the electrodes due to their large specific surface area, generally exhibiting superior electrochemical performances. However, it is worthy to point out that in present study, the contribution of porous characteristics of the LMO_x products on enhancing their electrochemical properties is limited because the synthesized $LMO_{7.0}$ and $LMO_{8.0}$ are not highly porous,

and both of them have a quite small specific surface area and low pore volume (Fig. S3, ESI†).

The trend of capacity retention for the LMO_x products would become amplified when cycled at a higher temperature of 55 ℃ (Fig. 5D) because the Mn dissolution becomes more severe at this temperature. At 55 ℃ with the same charging and discharging conditions as the room temperature tests, the $LMO_{7.0}$ also shows a good rate performance and thermal stability, and it retains 90.3 % of the initial capacity (109 mAh g^{-1}) after 60 cycles at the current rate of 1C, whereas $LMO_{8.5}$ exhibits an inferior rate capability at the high temperature, and it loses its capacity very rapidly as it only deliveries 41 mAh g^{-1} after 60 cycles. Moreover, the $LMO_{7.0}$ also shows robust thermal stability in the extended cycle number, as a high reversible capacity of 88 mAh g^{-1} (80.7 % retention) is still retained even after total 250 cycles.

In order to further reveal the reasons for the superior electrochemical properties of the synthesized LMO_x products, electrochemical impedance spectroscopy (EIS) measurements were performed with different samples as electrodes at the 1st cycle. As showed in Fig. 6A, the profile contains an intercept at Z'-axis in high-frequency region, a depressed semicircle in the intermediate-frequency region, and a straight line in the low-frequency region. The intercept at *Z'*-axis in the high frequency region represents the solution resistance (R_s), the depressed semicircle represents the charge transfer resistance (R_{ct}), and the sloping line in the low frequency region refers to diffusion-controlled Warburg impedance corresponding to the Li^+ ion diffusion in bulk material (R_w). It is noted that the R_{ct} value of the five samples gradually increase with the increase of pH value, in which $LMO_{7.0}$ has a minimum R_{ct} value of 251.3 Ω, while the maximum R_{ct} value of 1812.0 Ω is given by $LMO_{8.5}$. Accordingly, the stable discharge capacities delivered by $LMO_{7.0}$ electrode can be attributed to its relatively lower polarization rate developed within the electrode, whereas the higher charge transfer resistance inherent in $LMO_{8.5}$ electrode could lead to capacity decay upon its cycling at high current rate,[34] which is in agreement with the above electrochemical results.

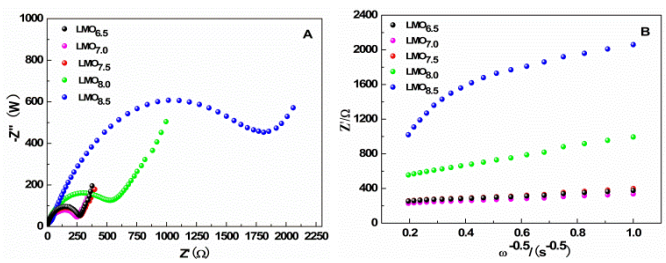

Fig. 6 (A) The electrochemical impedance spectra curves of LMO_x electrodes at the 1st cycle. (B) The relationship between Z' and $\omega^{-1/2}$ at low-frequency region.

Fig. 6B gives the relationship between *Z'* and $\omega^{-1/2}$ (the reciprocal square root of the low angular frequency). According to Eq. (1) $Z' = R_s + R_{ct} + \sigma_w \omega^{-1/2}$,[6] where σ_w is the Warburg factor, and the slopes of the plots in Fig. 6b indicate σ_w. Clearly, the Warburg factor drops in the order: $LMO_{7.0} < LMO_{6.5} < LMO_{7.5} < LMO_{8.0} < LMO_{8.5}$. During Li^+ ion intercalation/deintercalation process, the value of R_s is generally much smaller than that of R_{ct}, and thus the R_s can be ignored. Therefore, the depressed semicircle in the high frequency region can be mainly attributed to the charge transfer resistance.[35,36] Further, the Li diffusion coefficient is inversely proportional to the Warburg factor σ_w, that is, the diffusion coefficient of Li (D_{Li}) increases with the decreases of σ_w. As shown in Fig. 6B, the diffusion coefficient (D_{Li}) of LMO_x electrode increases from $LMO_{6.5}$ to $LMO_{7.0}$, and then decreases from $LMO_{7.0}$ to $LMO_{8.5}$. Accordingly, the $LMO_{7.0}$ electrode exhibits the largest Li diffusion coefficient, which implies its minimum Li^+ ion diffusion resistance. This observation indicates that such a unique truncated octahedral crystal structure of $LMO_{7.0}$ effectively reduces the barrier for Li^+-ion transfer at the electrode-electrolyte interface, thereby giving rise to a better discharge rate capability.

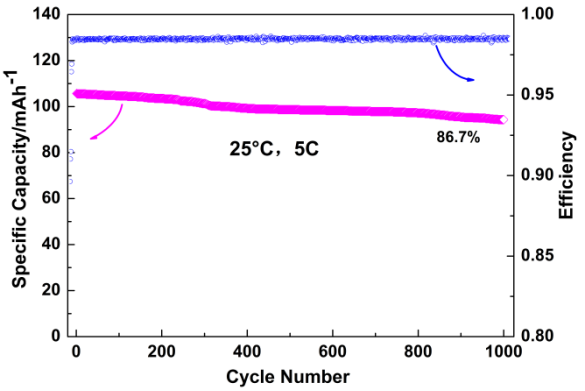

Fig. 7 Deep cycling performance of $LMO_{7.0}$ with 5C rate at 25 ℃.

The cycling stability of the resulting $LiMn_2O_4$ is further evaluated with long cycles. Fig. 7 presents the deep cycling performance of $LMO_{7.0}$ at a current rate of 5C. Attributed to the dominant {111} surfaces, $LMO_{7.0}$ exhibits an excellent cycling stability, maintaining 86.7% of its original capacity (108 mAh g^{-1}) after 1000 cycles, whilst the coulombic efficiency is retained to a high as ~99.5%. Fig. 8 shows the SEM image and XRD pattern of $LMO_{7.0}$ electrode after1000 cycles. It can be seen from Fig. 8A that after 1000 cycles, $LMO_{7.0}$ maintains its truncated octahedral morphology and the rougher surface is indicative of the formed SEI. Moreover, Fig. 8B compares the XRD patterns between the cycled electrode and fresh $LMO_{7.0}$ powder, which were normalized by the (311) peak. The cycled $LMO_{7.0}$ exhibits its spinel structure, although the XRD peaks from the cycled electrode marginally shifts to the right as compared to those of the fresh $LMO_{7.0}$ powder, probably due to the slight change of the lattice parameters. It is reasonable to expect that all the peaks would be weakened after the cycles because of the structure change and side reaction on the electrode/electrolyte interface. However, it can be seen from Fig. 8B that the spinel in the cycled electrode maintains the strongest intensity of the (111) peak observed from the fresh spinel. This demonstrates that the {111} crystal surfaces of the spinel is robust, while the predominant {111} surfaces endow $LMO_{7.0}$ with excellent cyclic stability.

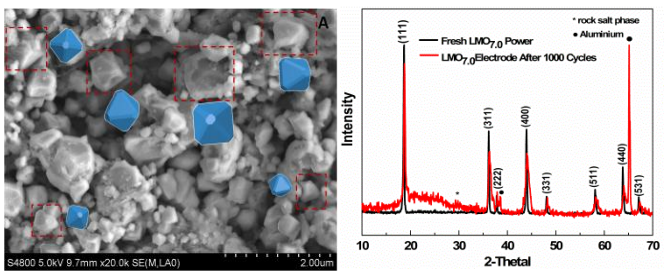

Fig. 8 (A) SEM image of $LMO_{7.0}$ electrode after 1000 cycles. (B) The corresponding XRD pattern compared with that of fresh $LMO_{7.0}$.

Conclusions

In summary, a series of single crystalline spinel $LiMn_2O_4$ deriving from spherical and cubic $MnCO_3$ as precursors have been successfully synthesized by developing a general and simple pH-mediated precipitation route. With careful pre-controls over the particle size and morphology of $MnCO_3$ precursors upon pH adjustment, $LiMn_2O_4$ with average size of 0.5-1.0 μm can be prepared through reaction between $LiOH{\cdot}H_2O$ and porous Mn_2O_3 spheres and cubes obtained from complete decomposition of $MnCO_3$ precursors. The $LiMn_2O_4$ prepared at pH value of 7.0 exhibits a well-defined truncated octahedral crystal structure, in which a small portion of the structure is truncated along the {110} orientations to support Li diffusion, while leaving most remaining surfaces aligned along the {111} crystalline orientations with minimal Mn dissolution. Due to the unique crystal structure, the synthesized $LiMn_2O_4$ as cathode material manifests superior rate capability and prolonged cycle stability, especially at elevated temperatures: the capacity retention of 86.7% after 1000 cycles at 5C rate under 25 ℃ and of 80.7% after 250 cycles with 1C rate under 55 ℃. These results demonstrate that in addition to the effect of synthetic temperature, the morphology of $MnCO_3$ as precursor prepared through the chemical precipitation approach also has a potential influence on the particle size and crystal structure of the resultant spinel $LiMn_2O_4$, as well as their electrochemical properties. This facile synthetic approach shows a great potential in large-scale industrial application toward developing higher energy density $LiMn_2O_4$ electrode materials together with longer life for LIBs.

Acknowledgements

The authors acknowledge the financial support from National Basic Research Program of China (973 program no. 2013CB934700) and the Sichuan Province Science and Technology Support Program (no. 2014GZ0093).

Notes and references

Address: Department of New Energy Materials, College of Materials Science and Engineering, Sichuan University, Chengdu 610064, China.
E-mail: hao.wu@scu.edu.cn and y_zhang@scu.edu.cn

†Electronic Supplementary Information (ESI) available: [Fig S1-S2]. See DOI: 10.1039/c000000x/

1 O. K. Park, Y. Y. Cho, S. H. Lee, H. C. Yoo, H. K. Son and J.Cho, *Energy Environ. Sci.*, 2011, **4**, 1621-1633.
2 A. S. Arico, P. Brue, B. Scrosati, and J. M. Tarascon, W. V. Schalkwijk, *Nat. Mater*., 2005, **4**, 366-377.
3 P. G. Bruce, B. Scrosati, and J. M. Tarason, *Angew. Chem. Int. Ed*., 2008, **47**, 9711-9716.
4 J. Zhu, K. Y. Zeng and L. Lu, *Electrochim. Acta.*, 2012, **68**, 52-59.
5 J. Xiao, X. L. Chen, P. V. Sushko, M. L. Sushko, L. Kovarik, J. J. Feng, Z. Q. Deng, J. M Zheng, G. L. Graff, Z. M. Nie, D. W Choi, J. Liu, J. G. Zhang and M. S. Whittingham, *Adv. Mater*., 2012, **24**, 2109-2116.
6 T. F. Yi, B. Chen, Y. R Zhu, X. Y. Li and R. S. Zhu, *J. Power Sources*, 2014, **247**, 778-785.
7 E. Hosono, T. Kudo, I. Honma, H. Matsuda and H. S. Zhou, *Nano Lett.*, 2009, **9**, 1045-1051.
8 J. Lu, Q. Peng, W. Y. Wang, C. Y. Nan, L. H Li and Y. D Li, *J. Am. Chem. Soc.*, 2013, **135**, 1649-1652.
9 C. H. Zheng, X. Liu, Z. F. Wu, Z. D. Chen and D. L. Fang, *Electrochim. Acta.*, 2013, **111**, 192-199.
10 S. Jayapal, R. Mariappan and S. Piraman, *J. Solid State Electrochem.*, 2013, **17**, 2157-2165.
11 Y. G. Li, B Tan and Y. Y. Wu, *Nano Lett.*, 2008, **8**, 265-270.
12 W. Y. Li, L. N. Xu and J. Chen, *Adv. Funct. Mater*., 2005, **15**, 851-857.
13 Y. Z. Wang, X. Shao, H. Y. Xu, M. Xie, S. X. Deng, H. Wang, J. B. Liu and H. Yan, *J. Power Sources*, 2013, **226**, 140-148.
14 C. Y. Zhu, G. Saito and T. Akiyama, *J. Mater. Chem. A*, 2013, **1**, 7077-7082.
15 Y. Ren, A. R. Armstrong, F. Jiao and P. G. Bruce, *J. Am. Chem. Soc*., 2009, **132**, 996-1004.
16 M. Okubo, E. Hosono, J. Kim, M. Enomoto, N. Kojima, T. Kudo, H. Zhou and I. Honma, *J. Am. Chem. Soc.*, 2007, **129**, 1444-1452.
17 Z. Yang, Y. Jiang, H. H. Xu and Y. H. Huang, *Electrochim. Acta*., 2013, **106**, 63-68.
18 T. J. Kun, W. F. Cheng, V. S. Battaglia and Z. H. Lang, *J. Electrochem. Sci*., 2014, **9**, 931-942.
19 D. C. Tang, Y. Sun, Z. Z. Yang, L. B. Ben, L. Gu and X. J. Huang, *Chem. Mater*., 2014, **26**, 3535-3543.
20 Y. C. Chen, K. Xie, Y. Pan and C. M. Zheng, *J. Power Sources.*, 2011, **196**, 6493-6497.
21 Y. G. Guo, J. S. Hu and L. J. Wan, *Adv. Mater.*, 2008, **20**, 2878-2887.
22 F. Jiao, J. L. Bao, A. H. Hill and P. G. Bruce, *Angew. Chem. Int. Ed*., 2008, **47**, 9711-9716.
23 H. K. Song, K. T. Lee, M. G. Kim, L. F. Nazar and J. Cho, *Adv. Funct.Mater.*, 2010, **20**, 3818-3834.
24 O. A. Shlyakhtin, S. H. Choi, Y. S. Yoon and Y. J. Oh, *Electrochim. Acta*., 2004, **50**, 511-516.
25 K. Suryakala, K. Marikkannu, G. P. Kalaignan and T.Vasudevan, Int. *J. Electrochem. Sci*., 2008, **3**, 136-144.
26 J. S. Kim, K. S. Kim, W. Cho, W. H. Shin, R. Kanno and J. W. Choi, *Nano Lett*., 2012, **12**, 6358-6365.
27 H. B. Lin, Y. M. Zhang, H. B. Rong, S. W. Mai, J. N. Hu, Y. H. Liao, L. D. Xing, M. Q. Xu, X. P. Li and W. S. Li, *J. Mater. Chem. A*, 2014, **2**, 9272-9279.
28 Y. L. Ding, J. Xie, G. S. Cao, T. J. Zhu, H. M. Yu and X. B. Zhao, *Adv. Funct. Mater.*, 2011, **21**, 348-355.
29 H. Jiang, T. Zhao, C. Yan, J. Ma, C. Li, *Nanoscale*, 2010, **2**, 2195-2198.
30 W. C. Huang, L. M. Lyu, Y. C. Yang, M. H. Huang, *J. Am. Chem. Soc*., 2011, **134**, 1261-1267.
31 L. G. Xiao, Y. L. Guo, D. Y. Qu, B. H. Deng, H. X. Liu and D. P. Tang, *J. Power Sources.*, 2013, **225**, 286-292.
32 C. H. Zheng, X. Liu, Z. F. Wu, Z. D. Chen and D. L. Fang, *Electrochim. Acta.*, 2013, **111**, 192-199.
33 M. Hirayama, H. Ido, K. Kim, W. Cho, K. Tamura, J. I. Mizuki, R. J. Kanno, *J. Am. Chem. Soc*., 2010, **132**, 15268-15276.
34 T. F. Yi, Y. Xie, Y. R. Zhu, R. S. Zhu and M. F. Ye, *J. Power Sources.*, 2012, **221**, 59-65.
35 J. Z. Zou, Y. Zhang, F. Wang, B. J. Chen, C. Lu and Z. Y. Wang, *J. Solid State Electrochem*., 2013, **9**, 2559-2565.
36 N. A. Milne, M. S. Kazaco and V. Luca, *J. Phys. Chem. C*, 2009, **113**, 12983-12995.
37 X. F. Li and C. L. Wang, *J. Mater. Chem. A*, 2013, **1**, 165-182.

38 Y. Zhao, X. F. Li, B. Yan, D. J. Li, S. Lawes and X. L. Sun, *J. Power Sources* 2015, **274**, 869
39 J. S. Zeng, M. S. Li, X. F. Li, C. Chen, D. B. Xiong, L. T. Dong, D. J. Li, A. Lushington and X. L. Sun, *App. Sur. Sci.* 2014, **317**, 884-891.
40 Y. F. Deng, Y. B. Zhou, Z. C. Shi, X. Zhou, X. Quan and G. H. Chen, *J. Mater. Chem. A*, 2013, **1**, 8170-8177.

